Nano Research
2022, 15(1): 669–676

ISSN 1998-0124 CN 11-5974/O4
https://doi.org/10.1007/s12274-021-3542-5

Research Article

Interplay between invasive single atom Pt and native oxygen vacancy in rutile TiO_2(110) surface: A theoretical study

Xiaoyang Wang[1], Liang Zhang[2], Yuxiang Bu[3], and Wenming Sun[1] (✉)

[1] *Department of Chemistry, China Agricultural University, Beijing 100193, China*
[2] *Dassault Systemes (Shanghai) Information Technology Co., Ltd., Shanghai 200120, China*
[3] *Department of Chemistry, Shandong University, Jinan 250100, China*

Received: 24 March 2021 / **Revised:** 22 April 2021 / **Accepted:** 26 April 2021

ABSTRACT

Oxygen vacancy (O_v) as well as O_v migration in metal oxide are of great importance in structural evolution of active center in single-atom catalysts (SACs). Here, the interplay between invasive single Pt atom and native O_v in SA-Pt/rutile TiO_2(110) surface, as well as their synergetic effect on water dissociation are investigated by density functional theory (DFT) calculations. We show that importing Pt atom as Pt-ads, Pt_{2c}, Pt_{5c} and Pt_{6c} modes could decelerate the O_v migration effectively, especially in Pt_{6c} mode. Under oxygen-rich conditions, Pt_{6c} substitution could make oxygen O_v formation easier, but migration harder. On $Pt_{6c}/Ti_{1-y}O_{2-x1}$(110) surface, as a bimetal center, Pt_{4c}–Ti_{5c} concave could not make water dissociation process easier; however, the O_{2c} closed to Pt become a good proton acceptor to make water dissociation on Ti_{5c}–O_{2c} more convenient with the aid of topmost Ti_{5c}.

KEYWORDS

oxygen vacancy, migration, rutile TiO_2, single-atom catalysts, density functional theory

1 Introduction

In the last decade, single-atom catalysts (SACs) have attracted world-wide research attention for performing distinct reactivity and selectivity [1–3]. SACs, which consist of single-dispersed atoms anchored onto metal oxide supports, achieved the maximum atom efficiency [4–13]. Generally, SACs could deactivate by sintering during the synthesis process, or in the process of the catalytic reaction [14]. Hence, the rational design of SACs with high thermal stability is vital to maximizing the utilization of precious metals. Despite the advances in sample preparation and characterization, fundamental understanding how active sites work or deactivate is still very challenging since the activity and selectivity depend on many factors, including but not limited to the reactive conditions (temperature, pressure, and humidity) and local environment of single metal atoms.

Although great efforts have been devoted to revealing the correlation between synthesis methods, active sites, and the catalysis performance in SACs [12], critical questions remain about the exact local structures of active sites as well as their dynamical evolution under reaction conditions. Growing evidences from both experimental and theoretical studies have determined the structures of active sites are dynamic, instead of static [15–18]. Wang et al. suggested that metal clusters will lose their original rigidity and evolve into dynamic species under reaction condition [19]. It should be noted that in some cases, the structural evolution does not necessarily cause the sintering of isolated atoms and instead only the local coordination environment together with the oxide states varies. Daelman confirmed the dynamic charge transfer between the metal and substrate [20]. DeRita et al. firstly correlated the coordination environment of the individual Pt atom with uniform coordination environments on metal oxide support with their chemical reactivities [21]. Tang et al. determined the response of single atom to different reaction conditions through performing density functional theory (DFT) calculations of Rh single atoms on rutile TiO_2(110) surface under various reaction conditions [22].

Titanium oxides are among the most common support materials utilized in SACs. SA-Pt/TiO_2 is a typically interfacial system which is catalytically active for a range of chemical reactions such as hydrosilylation reaction [23], diesel oxidation [24], selective hydrogenation [25], CO_2 reduction [26], water–gas shift reaction [27, 28], and photocatalysis reaction [29], etc. Pt can be stabilized by anchoring at specific site on TiO_2 support via atom-embedding or surface-adsorbing, which is similar to SA-Pt/CeO_2 or SA-Pt/Al_2O_3 [30–33]. For atom-embedding mode, TiO_2 separates and immobilizes isolated Pt by metal–support interactions [29]. Moreover, oxygen vacancies are readily formed on TiO_2 supports. The predominance of oxygen vacancy (O_v) in rutile TiO_2 [34–36] and anatase TiO_2 [37, 38] has been recognized for a long period. Furthermore, O_v migration is of great importance in catalyst structural evolution [39]. Hence, O_v as well as its migration on the TiO_2 support should be important factors that cannot be ignored when considering structural evolution of active sites in SA-Pt/TiO_2.

Consequently, several questions are raised naturally: As an intrinsic factor in the metal oxide support, how O_v as well as its migration affects the stability of isolated Pt. On the other hand, how invasive single Pt affects O_v's formation and migration process? Then, whether some new active centers

---

Address correspondence to swm@cau.edu.cn

would be formed via the interplay between invasive single Pt and native O_v.

Recently, Chen et al. reported a highly efficient photocatalyst by assembling single Pt atoms on defective TiO_2 support (SA-Pt/def-TiO_2). It was found that single Pt atoms as proton reduction sites promoted the neighboring TiO_2 units to generate surface oxygen vacancies [29]. In Chen's work, the interplay between imported single atom Pt and defective TiO_2 substrates was apparently beyond the studies between single atom and perfect substrates [23, 40] or reduced substrates with static O_v [41, 42], previously. Therefore, the evolution of Pt local environment during O_v migration should be taken into serious consideration for establishing more accurate structure–function relationships. To the best of our knowledge, the interplay of the two factors together with their synergic effect is seldom investigated. In our previous work [43], taking SA-Pt/anatase-TiO_2(101) as a prototype, we confirmed that introducing Pt could affect their neighboring O_v migration effectively. Furthermore, under their optimal conditions, Pt_{5c} and Pt_{6c} substitutions (Pt substituted topmost Ti_{5c} and Ti_{6c}, respectively) could make O_v formation easier. When Pt substituted either Ti_{5c} or Ti_{6c}, O_v tends to distribute around it and decreased its coordination number to 4. The adjacent bimetal Pt_{4c}–Ti_{4c} site in $Pt_{6c}/Ti_{1-y}O_{2-x1}$(101) can serve as an active center for water dissociation reaction [43].

To extend the scope of study from SAC/anatase-TiO_2 to SAC/rutile-TiO_2, in this work, SA-Pt/rutile-TiO_2(110) surface was selected as a case in point to answer the unknown questions and elucidate the interplay between invasive single atom Pt and native O_v as well as the synergic effect from a "quasi-dynamic" perspective.

2 Computational details

All spin-polarized DFT calculations were performed under the generalized gradient approximation (GGA) using revised Perdew–Burke–Ernzerhof (PBE) [44] functional. The core electrons were treated using DFT semi-core pseudopotential [45]. Double-numerical basis set plus *d*-functions (DND) was utilized to balance the accuracy and computational cost. A thermal smearing of 0.005 Ha (1 Ha = 27.211 eV) together with the direct inversion in an iterative subspace (DIIS) was applied to the orbital occupation to speed up self-consistent field (SCF) convergence. SCF tolerance was set to 1×10^{-6} Ha. During geometrical optimization and transition states searching, the convergence tolerances for energies, forces, and displacements were set to 1×10^{-5} Ha, 2×10^{-3} Ha/Å, and 5×10^{-3} Å, respectively.

Previous study has determined that GGA was reliable to describe the O_v migration in anatase TiO_2(110) surface by comparison with GGA + U calculations [46], hence only GGA was adopted in this work. The calculated lattice parameters of bulk rutile TiO_2 ($a = b = 4.692$ Å, $c = 2.996$ Å) agreed well with the experimental values ($a = b = 4.594$ Å, $c = 2.959$ Å) [47]. The corresponding $p(3 \times 1)$ TiO_2(110) surface was constructed. The slab contained three Ti_2O_4 layers, i.e., 36 O atoms and 18 Ti atoms. A 15 Å vacuum layer between the images along the direction of the surface normal was utilized. To consider the vacancy migration along the slab, during the optimization, all three Ti_2O_4 layers and the adsorbents were fully relaxed. Dipole correction was adopted in all calculations. The first Brillouin zone integration was sampled with Γ-centered $2 \times 2 \times 1$ k-point mesh for $p(3 \times 1)$ rutile TiO_2(110) surface. A combination of the linear synchronous transit and the quadratic synchronous transit method (LST/QST) [48] was used to locate the transition state. Geometrical optimization and transition states searching were performed by using the DMol3 program [41, 42].

To explore the formation feasibility of the corresponding models under different conditions (oxygen-rich or oxygen-poor), the formation energy (E_{form}) was calculated using the following formula

$$E_{\mathrm{form}} = E_{\mathrm{Pt/Ti_{1-\mathit{y}}O_{2-\mathit{x}1}}} + \mu_{\mathrm{Ti}} + \mu_{\mathrm{O}} - (\mu_{\mathrm{Pt}} + E_{\mathrm{TiO_2}})$$

where $E_{\mathrm{Pt/Ti_{1-\mathit{y}}O_{2-\mathit{x}1}}}$ and $E_{\mathrm{TiO_2}}$ are the total energies of doped and stoichiometric TiO_2 models. The former includes the four configurations, where both invasive single atom Pt and native O_v are introduced. μ_{Ti}, μ_{O}, and μ_{Pt} are the chemical potentials for Ti, O, and Pt, respectively. μ_{O} under oxygen-rich condition was estimated by $\mu_{\mathrm{O}} = 1/2\mu_{\mathrm{O_2}}$, and the chemical potential of Ti was calculated by $\mu_{\mathrm{Ti}} = \mu_{\mathrm{TiO_2}} - 2\mu_{\mathrm{O}}$. Meanwhile, under oxygen-poor condition, chemical potential of Ti was calculated by $\mu_{\mathrm{Ti}} = \mu_{\mathrm{Ti}}^{\mathrm{metal}}$, and the chemical potential of O was calculated by $\mu_{\mathrm{O}} = 1/2(\mu_{\mathrm{TiO_2}} - \mu_{\mathrm{Ti}})$. Pt as an adsorbate or substitutional dopant, the chemical potential was $\mu_{\mathrm{Pt}}^{\mathrm{metal}}$, in both conditions as suggested by Luo et al. [49].

Electronic properties calculations of selected structures were performed with GGA/PBE functional with ultrasoft pseudopotentials supplied by standard solid-state pseudopotentals (SSSP) [50, 51] with Quantum Espresso [52, 53]. Since DFT + U approach introduces as on-site correction to produce better band gap in semiconductor with localized *d* or *f* electrons [54], Deskins et al. suggested that the reasonable gap states occur for *U* values between 3.3 and 4.1 eV [55]. Here, 3.3 eV was selected for the localized 3*d* electrons correction of Ti. A refine Monkhorst–Pack k-point grid used was 6 × 8 × 1, and the kinetic energy cutoffs for wave-functions and charge density were 40 and 400 Ry, respectively. To analyze and visualize the hydrogen bonds between adsorbate and substrate on selected systems, the noncovalent interaction index approach developed by Johnson et al. was adopted [56]. In this approach, the reduced density gradient together with the electron density was used to distinguish the covalent and noncovalent interactions. The detailed analysis process could refer to the previous works [56–58].

3 Results and discussion

3.1 Oxygen vacancy migration in rutile TiO_{2-x}(110) surface

As show in Fig. 1(a), the upmost atoms on the stepped stoichiometry rutile TiO_2(110) surface are 2-fold (O_{2c}) and 3-fold (O_{3c}) coordinated oxygen as well as 5-fold (Ti_{5c}) and 6-fold (Ti_{6c}) coordinated titanium. Firstly, the preference sites of oxygen vacancies on TiO_2 substrate were investigated. Due to the symmetry of the model adopted here, five sites (labeled from I to V, as shown in Figs. 1(a) and 1(b)), are selected to settle oxygen vacancies. Sites I, II, and IV are in the 1st TiO_2 tri-layer, and meanwhile, sites III and V are in the 2nd TiO_2 tri-layer. These TiO_{2-x}(110) configurations were optimized, while the corresponding total energies were compared. Results indicated that the most preference oxygen vacancy site was I, where the topmost O_{2c} was removed. O_{3c} site (II) beneath site I was the second preference site with a small energy difference (11.7 kcal/mol) compared with configuration I. It should be noted that O_v on IV is not an energetic favorable site. Consequently, it seems not to be reasonable to construct O_v on site IV and make it as an anchoring site for single Pt atom as suggested in the previous work [59]. Migration paths of oxygen vacancies are considered mainly in two modes: inter-layer migration (II–III and IV–V) and intra-layer migration (V–III, I–II, and I–IV). As shown in Fig. 2, intra-layer migrations along I–IV need

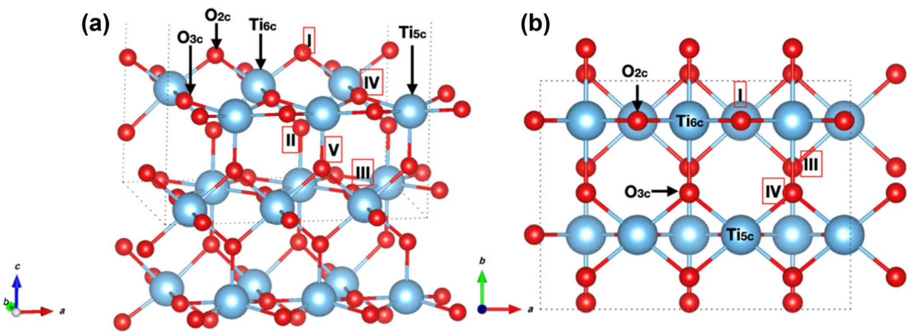

Figure 1 Side (a) and top (b) views of clean rutile $TiO_2(110)$ surface model adopted in this work. Possible oxygen vacancy sites are labeled from I to V. Meanwhile, the upmost atoms with different coordination numbers are also denoted. Red and indigo spheres represent the O and Ti atoms, respectively.

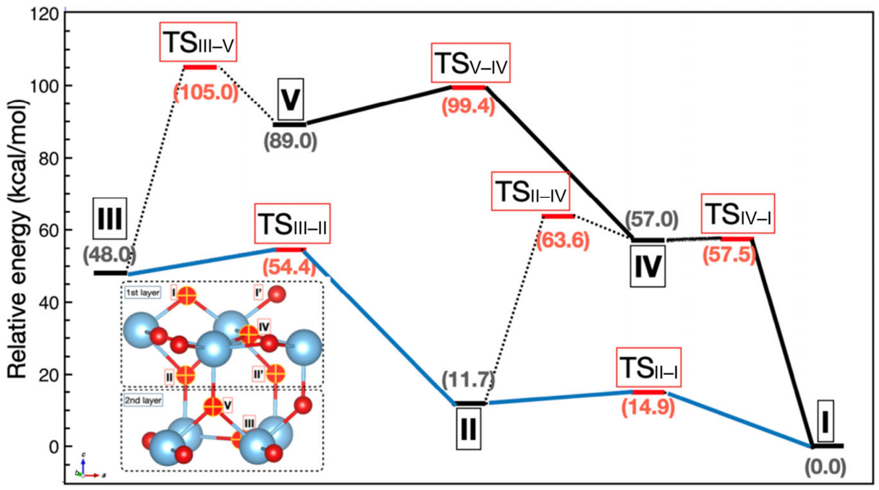

Figure 2 Energy profile of possible O_v migration between adjacent sites along both intra-layer and inter-layer paths in rutile $TiO_{2-x}(110)$ surface. Oxygen vacancy on site I is the most stable configuration, hence the total energy of configuration I is set as the reference. The inset shows possible O_v sites along their migration paths. Relative energies of each species along reaction coordinate are labeled. Red and indigo spheres represent the O and Ti atoms, respectively.

to overcome a barrier of about 57.5 kcal/mol, which is the highest barrier among the considered paths. Furthermore, this migration path is a highly endothermic process. Therefore, this O_v migration step is determined as both thermodynamically and kinetically unfavorable. It should be noted that the migration barriers of IV–I and IV–II are very low (only 0.5 and 6.6 kcal/mol, respectively). That is to say, even if formed, oxygen vacancy on site IV would migrate to site I or II facilely. It was verified once again that the topmost O_{3c} site (IV) is hard to form O_v or be involved in O_v migration.

Migration lengths of the steps in Fig. 2 are listed in Table S1 in the Electronic Supplementary Material (ESM). O_v migration between V and II is omitted since the distance between sites V and II is 3.382 Å, which is significantly longer than the others. Based on the scanning tunneling microscope images and DFT calculation, Zhang et al. determined that the O_v diffusion barrier along the bridge-boned oxygen vacancy (BBO_v, labeled as site I in this work) arrow was 26.5 and 23.8 kcal/mol, respectively [60]. In our model, two parallel migration barriers along the [001] direction form I’ to I and from II’ to II is 29.8 and 38.5 kcal/mol, respectively. Hence, two independent O_v migration paths (I–II–III and I–IV–V) exist from the surface to the inner. Relative energies indicate that O_v formation on site V is harder than that on site III. Meanwhile, in the reduced TiO_{2-x} surface, the oxygen vacancy prefers to locate on surface site I and subsurface site II. Consequently, the migration path along I–II–III, which connects the most stable oxygen vacancy sites is focused in the following part.

In our previous study, we have determined the coupling between native O_v and invasive Pt atom in anatase $TiO_{2-x}(101)$ surface [43]. Similarly, we considered four single atom Pt sites according to the previous study, which were Pt-ads, Pt_{2c}, Pt_{5c}, and Pt_{6c}. Pt-ads denotes the configuration where Pt is adsorbed on the rutile $TiO_2(110)$ surface. Pt_{2c}, Pt_{5c}, and Pt_{6c} represent the configurations where Pt substituted the topmost O_{2c}, Ti_{5c}, and Ti_{6c} of the surface, respectively. The migration barrier height from II to III (42.7 kcal/mol) is very high, indicating this migration step is kinetically unfavorable. Only the migration barrier height from I to II (14.9 kcal/mol) is selected as a benchmark to estimate the contribution of Pt in accelerating or decelerating the O_v migration.

3.1.1 *Oxygen vacancy migration in Pt-ads/$TiO_{2-x1}(110)$ surface*

Several Pt adsorption configurations were considered firstly on stoichiometry rutile $TiO_2(110)$ surface, as shown in Fig. S1 in the ESM. Single Pt atom prefers to occupy the hollow site among O_{2c}, Ti_{5c}, and two O_{3c} atoms, forming an O_{2c}–Pt–Ti_{5c} motif which is consistent with the previous results [59]. The distances of Pt–O_{2c} and Pt–Ti_{5c} are 1.984 and 2.466 Å, respectively. As a starting point, this configuration is selected to construct the Pt-ads/$TiO_{2-x1}(110)$ surface and investigate the oxygen vacancy migration inside.

According to our previous study [43], in Pt-ads/anatase-$TiO_2(101)$ structure, if one oxygen vacancy is formed on O_{2c} which is formally part of the bridge to support the single atom Pt, Pt atom will move to refill the vacancy and form a Ti_{6c}–Pt–Ti_{5c} motif on the surface spontaneously. However, on rutile $TiO_2(110)$ surface, if the O_{2c} atom which connects with Pt is removed, Pt atoms will not refill the O_{2c} site. On the contrary, Pt will move to the top of Ti_{5c}. O_v on the rutile $TiO_2(110)$

surface is not a good anchoring site for Pt, which is different from the performance of O_v on anatase $TiO_2(101)$ surface [61]. In this model, due to their relative locations to the anchoring Pt, two O_v migration paths (I–II–III and i–ii–iii) were considered. The relative energies and the migration barriers are marked in Fig. 3(a). Among the six O_v sites, surface site I is still the most stable one, which is 0.3 kcal/mol lower than site i. In other words, Pt adsorption on rutile $TiO_2(110)$ surface does not alter the preference-site of O_v. The relative energies as well as the migration barriers along the two paths are similar. In this model, the energy differences between subsurface O_v and surface O_v are lower than their counterpart in clean rutile $TiO_2(110)$ surface (7.4–7.5 vs. 11.7 kcal/mol). Moreover, the migration barriers between surface O_v and subsurface O_v are higher than their counterpart in clean rutile $TiO_2(110)$ surface (16.3–17.2 vs. 14.9 kcal/mol). The migration barriers between subsurface O_v and inner sites are higher than their counterpart in clean rutile $TiO_2(110)$ surface (45.2–48.0 vs. 42.7 kcal/mol). The kinetic information suggests that Pt-adsorption would hinder the O_v migration from surface to subsurface and inner slightly.

3.1.2 *Oxygen vacancy migration in $Pt_{2c}/TiO_{2-x2}(110)$ surface*

Firstly, one O_{2c} was replaced by Pt atom to construct $Pt_{2c}/TiO_{2-x1}(110)$. The distances between Pt and its neighboring Ti atom is 2.584 Å. Notably, two oxygen atoms are removed here (labeled as $Pt_{2c}/TiO_{2-x2}(110)$) while only one is removed in Pt-ads/$TiO_{2-x1}(110)$ surface. In this model, the most stable O_v site is still on O_{2c}, which is the same as in clean surface and Pt-ads/$TiO_2(110)$ surface. Since one O_{2c} is substituted by one Pt atom, there is only one complete path along I–II–III. As shown in Fig. 3(b), the migration barrier of I–II step is similar to that in Pt-ads/$TiO_{2-x1}(110)$ surface (18.8 vs. 16.3–17.2 kcal/mol), while it is larger than its counterpart in Pt-free/$TiO_{2-x1}(110)$ surface (18.8 vs. 14.9 kcal/mol). Interestingly, the barrier of step II–ii along [001] is 53.4 kcal/mol, which is larger than that in step II–III or II–iii. Considering the relative energies of III and iii, as well as the barriers of II–III and II–iii, path II–iii is slightly favorable. Therefore, the reasonable O_v migration path is I–II–iii. That is to say, O_{3c} beneath Pt_{2c} would be intact during the O_v migration process. The migration barriers between subsurface O_v and inner sites are higher than their counterparts in clean rutile $TiO_2(110)$ surface (48.7–49.6 vs. 42.7 kcal/mol). Thus, in this model, replacing O_{2c} by Pt would hinder the O_v migration from surface to subsurface and inner slightly.

3.1.3 *Oxygen vacancy migration in $Pt_{5c}/Ti_{1-y}O_{2-x1}(110)$ surface*

When the single Pt atom substituted one Ti_{5c} on the surface, the corresponding migration processes showed some new features. Firstly, the distance between Pt and its beneath O atom is 2.652 Å, which is significantly longer than that between Pt and O_{3c} atom on the surface (2.017–2.018 Å). Apparently, Pt adopts a four coordinated configuration, instead of a five coordinated configuration as adopted in Ti_{5c}. Similar phenomenon in Pt_{5c}/anatase-$Ti_{1-y}O_2(101)$ surface was also observed in our previous study [43]. In this model, the most stable O_v site is I, which is the topmost O_{2c} far away from Pt_{5c}. Migration from site I to i needs to climb a barrier of 43.0 kcal/mol. Forming O_v on O_{2c} close to Pt_{5c} is 2.9 kcal/mol less stable than that on site I. As shown in Fig. 4(a), several migration paths were considered. Migration processes from the subsurface (site II) to the inner (sites iii and III) are still harder compared with that in Pt-free $TiO_{2-x}(110)$ surface (47.4–49.4 vs. 42.7 kcal/mol).

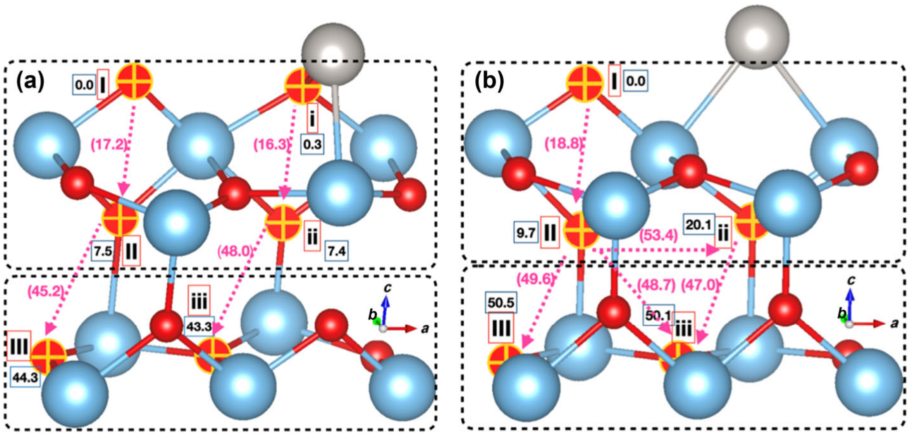

Figure 3 Possible O_v migration paths between adjacent sites for (a) Pt-ads/$TiO_{2-x1}(110)$ surface and (b) $Pt_{2c}/TiO_{2-x2}(110)$ surface. Relative energies and barriers of each species along the reaction coordinate are marked with black and pink numbers, respectively. Red, indigo, and silver spheres represent the O, Ti, and Pt atoms, respectively.

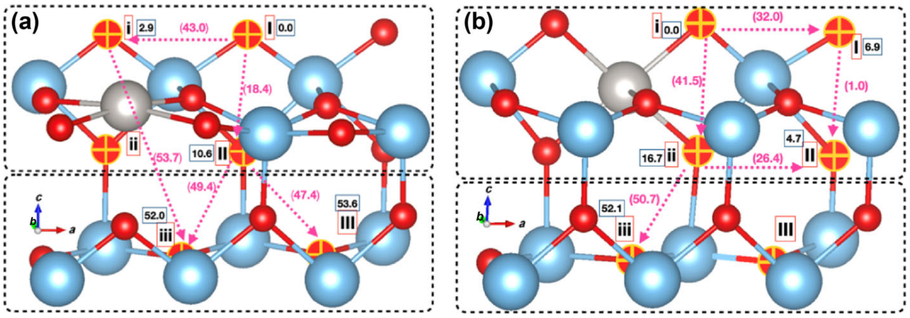

Figure 4 Possible O_v migration paths between adjacent sites for (a) $Pt_{5c}/Ti_{1-y}O_{2-x}(110)$ surface and (b) $Pt_{6c}/Ti_{1-y}O_{2-x}(110)$ surface. Relative energies and barriers of each species along the reaction coordinate are marked with black and pink numbers, respectively. Red, indigo, and silver spheres represent O, Ti, and Pt atoms, respectively.

Meanwhile, the migration process between II and I is harder compared with that in Pt-free $TiO_{2-x}(110)$ surface (18.4 vs. 14.9 kcal/mol). Interestingly, along the i–ii–iii path, oxygen vacancy at ii site is unstable, while it will convert to i after geometry optimization. The migration step of i–iii is a significant endothermic process with a high barrier height, which makes i–iii an inactive O_v migration path. In this model, the effect of Pt_{5c}-substitution is also to hinder the O_v migration from surface to subsurface and inner slightly, which is similar to the Pt-ads and Pt_{2c}-substitution.

3.1.4 *Oxygen vacancy migration in $Pt6c/Ti_{1-y}O_{2-x1}(110)$ surface*

Firstly, one Ti_{6c} was replaced by Pt to form the $Pt_{6c}/Ti_{1-y}O_2(110)$ surface. The distances between Pt and its six neighboring oxygen atoms are about 2.081–2.092 Å, indicating its 6-coordinated character. Then, one oxygen atom was removed to build the corresponding $Pt_{6c}/Ti_{1-y}O_{2-x1}(110)$ surface configuration. From Fig. 4(b), we can find that although site i is the most stable location for O_v, the corresponding migration path i–ii–iii is very hard. The barrier of i–ii is almost three times higher than that in Pt-free/$TiO_{2-x1}(110)$ surface (41.5 vs. 14.9 kcal/mol), while the barrier of O_v migration along (001) direction (from i to I) is 32.0 kcal/mol. These high barriers suggest that O_v migration along i–ii or i–I is extremely difficult. In this model, when O_v was formed on its most stable site, Pt was supposed to be coordinated with the last remaining five oxygen atoms. However, the longest distance between Pt and its fifth closest oxygen atoms is 2.564 Å, which is significantly longer than the other Pt–O_{2c} and Pt–O_{3c} (2.006–2.082 Å). Apparently, the coordination number of Pt in $Pt_{6c}/Ti_{1-y}O_{2-x1}(110)$ surface is 4 in its most stable configuration. It is interesting to note that O_v on surface site I is less stable than on subsurface site II, which is different from both Pt-free/$TiO_{2-x1}(110)$ surface, Pt-ads/$TiO_{2-x1}(110)$ surface, $Pt_{2c}/TiO_{2-x2}(110)$ and $Pt_{5c}/Ti_{1-y}O_{2-x1}(110)$ surface. Such inversion caused by Pt-substitution was also detected in Pt_{6c}/anatase-$Ti_{1-y}O_{2-x1}(101)$ surface[43]. Meanwhile, O_v could not occupy site III. Oxygen atom at II will refill vacancy on site III spontaneously after geometry optimization. O_v migration along I–II only needs to climb a barrier of 1.0 kcal/mol, while O_v migration along II–ii needs to overcome a barrier of 38.4 kcal/mol. It is well known that detecting the sites of second or third O_v in surface is extremely cumbersome due to the low symmetry. Herein, these results might offer us a clue to filter the site of second O_v in this model. In short, $Pt_{6c}/Ti_{1-y}O_{2-x1}(110)$ exhibits a remarkable feature: Vacancy prefers to occupy site i on surface near Pt, while it is almost immobile due to the huge migration barrier from i to ii.

4 Discussion

Till now, we could achieve the conclusion that introducing Pt atom as Pt-ads, Pt_{2c}, Pt_{5c}, and Pt_{6c} modes could decelerate the O_v migration effectively, especially in Pt_{6c} mode.

When Pt substituted $Ti_{5c,}$ O_{3c} beneath Pt would downward shift to elongate Pt–O distance (2.652 Å), forming a planar Pt–O 4-fold coordinated configuration, as shown in Fig. 5(a). It is interesting when Pt substituted Ti_{6c}, O_v tended to distribute around it and decreased its coordination number to 4, leading a nearly planar Pt–O 4-fold coordinated configuration. Meanwhile, the next O_v would not prefer to distribute around 4-coordinated Pt and decrease its coordinate number further. That is to say, on TiO_2 surface, the substituted Pt could adopt either a nearly planar Pt–O 4-fold coordinated configuration or an octahedral Pt–O 6-fold coordinated configuration no matter whether it is reduced or stoichiometric, as shown in Fig. 5. This would be an important clue for fitting element selective X-ray absorption fine structure (XAFS) results, or identifying the dynamical coordinate structure of active center.

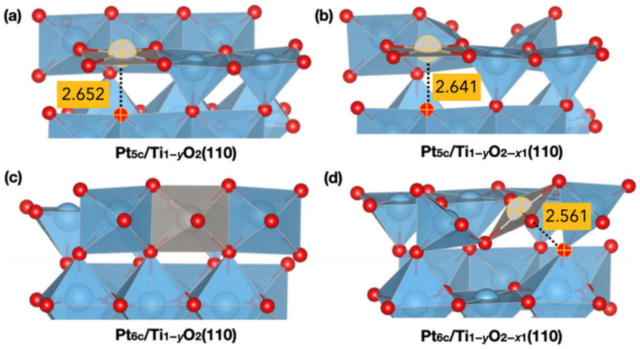

Figure 5 Polyhedral style of surface configurations such as (a) $Pt_{5c}/Ti_{1-y}O_2(110)$, (b) $Pt_{5c}/Ti_{1-y}O_{2-x1}(110)$, (c) $Pt_{6c}/Ti_{1-y}O_2(110)$, and (d) $Pt_{6c}/Ti_{1-y}O_{2-x1}(110)$. The farthest Pt–O distances around the Pt were highlighted. Red, indigo, and silver spheres represent O, and Ti atoms, and Pt atoms, respectively.

In previous studies, it has been proposed that defects on the support are necessary to induce a strong metal–support interaction (SMSI) [62–66]. In order to investigate the feasibility of the Pt-O_v coexisted TiO_2 surfaces, the formation energies of the corresponding structures were calculated and shown in Fig. 6. We can find a selectivity of these four structures under different conditions. That is, oxygen-poor condition is beneficial for forming Pt-ads/$TiO_{2-x1}(110)$ and $Pt_{2c}/TiO_{2-x2}(110)$, whereas oxygen-rich condition is beneficial for forming $Pt_{5c}/Ti_{1-y}O_{2-x1}(110)$ and $Pt_{6c}/Ti_{1-y}O_{2-x1}(110)$. Under oxygen-poor condition, Pt-ads/$TiO_{2-x1}(110)$ is feasible no matter Pt-adsorption or surface O_v formation is achieved firstly. Furthermore, the pre-adsorbed Pt on $TiO_2(110)$ surface makes O_v formation (−5.01 vs. −5.70 eV) harder under oxygen-poor condition. Similarly, under oxygen-poor condition, $Pt_{2c}/TiO_{2-x2}(110)$ is also feasible no matter Pt-substitution or subsurface O_v formation is achieved firstly. Meanwhile, the pre-substituted Pt_{2c} on surface has tiny effect on O_v formation (−5.54 vs. −5.70 eV) under oxygen-poor condition. The effect from Pt is different from that on anatase $TiO_2(101)$ surface, where pre-adsorbed Pt or pre-substituted Pt_{2c} atom on surface has no effect on O_v formation under oxygen-poor condition [43]. Under oxygen-rich condition, Pt substitution firstly in $Pt_{5c}/Ti_{1-y}O_{2-x1}(110)$ and $Pt_{6c}/Ti_{1-y}O_{2-x1}(110)$ is preferred than the formation of oxygen vacancies. Based on these pre-substituted configurations, O_v formation is endothermic. However, the endothermic process is still more facile than the O_v formation on pure TiO_2 under oxygen-rich condition (0.59 vs. 0.89 eV for $Pt_{6c}/Ti_{1-y}O_{2-x1}(110)$). Our results are consistent with the previous work, which confirmed that metal species on reducible oxides thermodynamically prefer cation replaced positions in the oxide support lattice under oxidizing environments [14, 15, 21]. These results indicate that under their optimal conditions, Pt_{6c} substitution could make oxygen O_v formation easier, Pt-adsorption could make O_v formation harder, while Pt_{5c} and Pt_{2c} substitutions show tiny effect on O_v formation.

The formation energies calculation determined that Pt_{6c} substitution could make oxygen O_v formation easier (Fig. 6(d)). Meanwhile, the O_v migration path analysis determined that Pt_{6c} could make O_v immobile (Fig. 4(b)). The thermodynamic together with kinetic information suggests configuration i of $Pt_{6c}/Ti_{1-y}O_{2-x1}(110)$ is the dominant configuration. In this configuration, the distance between exposed Ti_{5c} and Pt_{4c} is 3.175 Å, which is longer than the Pt–Ti bond lengths in some Ti-Pt intermetallic (2.861 Å in TiPt, 2.773 Å in $TiPt_8$, and 2.819 Å in Ti_3Pt) [43]. It is interesting to explore whether this adjacent bimetal open structure could serve as an active site

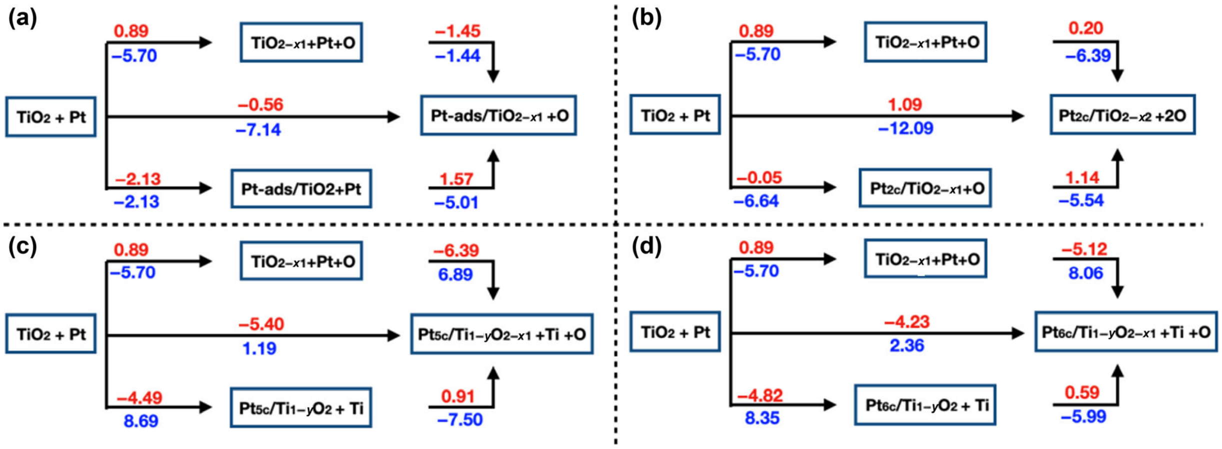

Figure 6 Schematic illustration for the formation procedures of Pt-O_v coexisted TiO_2 surfaces. The calculated formation energies (E_{form}, units: eV) obtained under oxygen-rich and oxygen-poor conditions are shown in red and blue, respectively.

for some catalytic reactions.

Taking water dissociation as an example, TiO_2(110) surface, TiO_{2-x}(110) surface, as well as $Pt_{6c}/Ti_{1-y}O_{2-x1}$(110) surface were chosen to estimate the activity. Upon adsorption, oxygen atom from water molecule prefers to locate on the top of Ti_{5c}, while one OH bond points to one O_{2c} on TiO_2(110) surface. O_{2c} is involved in the dissociation process via forming H-bonds and accepting a proton. Ti_{5c}–O_{2c} as one reaction center to dissociate O–H bond exists on TiO_2(110) surface, TiO_{2-x}(110) surface, as well as $Pt_{6c}/Ti_{1-y}O_{2-x1}$(110) surface. Distances of O_{water}–Ti_{5c} are 2.240, 2.320 and 2.242 Å on TiO_2(110), TiO_{2-x}(110), and $Pt_{6c}/Ti_{1-y}O_{2-x1}$(110) surface, respectively. The shorter O_{water}–Ti_{5c} distances indicate stronger binding strength on TiO_2(110) and $Pt_{6c}/Ti_{1-y}O_{2-x1}$(110) surface. As shown in Fig. 7, the dissociation processes at Ti_{5c}–O_{2c} center on TiO_2(110) surface and $Pt_{6c}/Ti_{1-y}O_{2-x1}$(110) surface are exothermic with reaction energy of −13.9 and −9.3 kcal/mol, respectively. The dissociation barriers are 6.3 and 5.0 kcal/mol on TiO_2(110) surface and $Pt_{6c}/Ti_{1-y}O_{2-x1}$(110) surface, respectively. However, on TiO_{2-x}(110) surface, water dissociation process at Ti_{5c}–O_{2c} is endothermic together with a high reaction barrier (15.2 kcal/mol). These results suggest that the activity to accept proton in water follows the trend: O_{2c} close to Pt > O_{2c} in pristine surface > O_{2c} close to O_v. The geometrical parameters for hydrogen bonds in these three models are listed in Table S7 in the ESM. We can find that H_2O-$Pt_{6c}/Ti_{1-y}O_{2-x1}$ model exhibits the strongest adsorbate-substrate hydrogen-bond with the shortest H_{water}–O_{2c} distance and largest O_{water}-H_{water}-O_{2c} angle. Furthermore, the reduced gradient density (RDG) plots in Figs. 8(d) and 8(e) also confirm the strength trend of hydrogen bonds. The best affinity to accept proton for O_{2c} in $Pt_{6c}/Ti_{1-y}O_{2-x1}$ model should be attributed to the significant *p*-like orbital of O_{2c} to the highest occupied molecule orbital (HOMO) as shown in Fig. 8(c). On TiO_{2-x}(110) and $Pt_{6c}/Ti_{1-y}O_{2-x1}$(110) surface, removing one oxygen atom on O_{2c} leads to bimetal centers such as Ti_{5c}–Ti_{5c} and Pt_{4c}–Ti_{5c}, respectively. We also considered the water dissociation processes on these bimetal centers. As shown in Fig. 7, the adsorption energies for water on both Ti_{5c}–Ti_{5c} and Pt_{4c}–Ti_{5c} centers are lower than that on Ti_{5c}–O_{2c} center, indicating weaker interactions. Although these dissociation processes are exothermic, they suffer higher dissociation barriers compared with that on Ti_{5c}–O_{2c} center. Especially on $Pt_{6c}/Ti_{1-y}O_{2-x1}$(110) surface, as shown in Fig. S2 in the ESM, water molecule prefers to locate in the concave O_{2c}–Pt_4–O_{3c}–Ti_{5c}–O_{2c} near Ti_{4c} side, hence accepting proton in water by O_{2c} close to Ti_{5c} is easier than that by O_{2c} close to Pt_{4c}. HOMO plots (Figs. 8(a)–8(c)) reveal that although *d*-like orbital from Pt in $Pt_{6c}/Ti_{1-y}O_{2-x1}$ model exposed, the top-down alternate anion–cation (O_{2c}–Pt_{4c}) arrangement and the steric effect caused by the O_{2c}–Pt_4–O_{3c}–Ti_{5c}–O_{2c} concave prohibit negative center of water molecule approaching Ti_{4c} site. In summary, on $Pt_{6c}/Ti_{1-y}O_{2-x1}$(110) surface, as a bimetal center Pt_{4c}–Ti_{5c} concave could not make water dissociation process easier; however, O_{2c} closed to Pt becomes a good proton acceptor to make water dissociation on Ti_{5c}–O_{2c} more convenient with the aid of topmost Ti_{5c}.

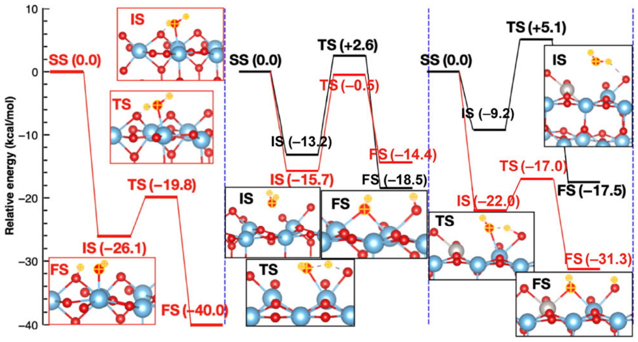

Figure 7 Typical water dissociation pathways on (a) TiO_2(110) surface, (b) TiO_{2-x}(110) surface, as well as (c) $Pt_{6c}/Ti_{1-y}O_{2-x1}$(110) surface. IS, TS, and FS denote the initial state, transition state, and final state, respectively. The relative energies are marked in parentheses (units: kcal/mol), while the reference energy is that of the separate states.

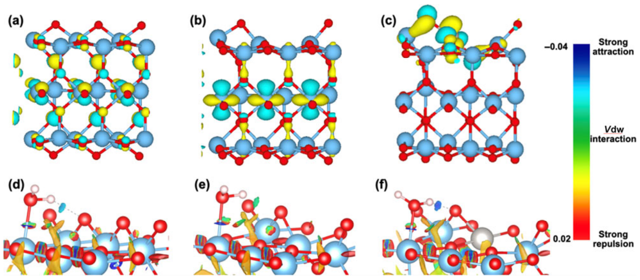

Figure 8 Isosurface plots ($s = 0.002\alpha_0^{-3}$, α_0: Bohr radius) of HOMO of (a) TiO_2(110) surface, (b) TiO_{2-x}(110) surface, as well as (c) $Pt_{6c}/Ti_{1-y}O_{2-x1}$(110). Reduced density gradient ($s = 0.35\alpha_0^{-3}$) for (d) H_2O-TiO_2(110) surface, (e) H_2O-TiO_{2-x}(110) surface, as well as (f) H_2O-$Pt_{6c}/Ti_{1-y}O_{2-x1}$(110) surface. The isosurfaces of the RDG in the bottom plots are colored according to the values of the quantity sign (λ_2)ρ, and the RGB scale is indicated.

5 Conclusions

In summary, we have studied the interplay between invasive Pt and native O_v on rutile TiO_2 surface as well as their synergetic effects on water splitting. It is found that O_v prefers to occupy surface O_{2c} site. Introducing Pt atom as Pt-ads, Pt_{2c}, Pt_{5c}, and Pt_{6c} modes could decelerate the O_v migration effectively, especially in Pt_{6c} mode. Oxygen-poor condition is beneficial for forming Pt-ads/TiO_{2-x1}(110) and Pt_{2c}/TiO_{2-x2}(110), whereas oxygen-rich condition is beneficial for forming Pt_{5c}/$Ti_{1-y}O_{2-x1}$(110) and Pt_{6c}/$Ti_{1-y}O_{2-x1}$(110). Under their optimal conditions, Pt_{6c} substitution could make oxygen O_v formation easier; Pt-adsorption could make O_v formation harder, while Pt_{5c} and Pt_{2c} substitutions show tiny effect on O_v formation. When Pt substitutes either Ti_{5c} or Ti_{6c}, the O_v tends to distribute around it and decreases its coordination number to 4. On Pt_{6c}/$Ti_{1-y}O_{2-x1}$(110) surface, as a bimetal center, Pt_{4c}–Ti_{5c} concave could not make water dissociation process easier; however, O_{2c} closed to Pt becomes a good proton acceptor to make water dissociation on Ti_{5c}–O_{2c} more convenient with the aid of topmost Ti_{5c}. These results can provide a "quasi-dynamic" perspective to understand the structural-active evolution of single atom supported on metal oxide surfaces.

Acknowledgements

This work is supported by the 2115 Talent Development Program of China Agricultural University.

Electronic Supplementary Material: Supplementary material (covergence test for K-points, water dissociation pathways as well as the water diffusion paths on selected surfaces) is available in the online version of this article at https://doi.org/10.1007/s12274-021-3542-5.

References

[1] Qiao, B. T.; Wang, A. Q.; Yang, X. F.; Allard, L. F.; Jiang, Z.; Cui, Y. T.; Liu, J. Y.; Li, J.; Zhang, T. Single-atom catalysis of CO oxidation using Pt1/FeO_x. *Nat. Chem.* 2011, *3*, 634–641.

[2] Yang, X. F.; Wang, A. Q.; Qiao, B. T.; Li, J.; Liu, J. Y.; Zhang, T. Single-atom catalysts: A new frontier in heterogeneous catalysis. *Acc. Chem. Res.* 2013, *46*, 1740–1748.

[3] Wang, A. Q.; Li, J.; Zhang, T. Heterogeneous single-atom catalysis. *Nat. Rev. Chem.* 2018, *2*, 65–81.

[4] Lin, L. L.; Zhou, W.; Gao, R.; Yao, S. Y.; Zhang, X.; Xu, W. Q.; Zheng, S. J.; Jiang, Z.; Yu, Q. L.; Li, Y. W. et al. Low-temperature hydrogen production from water and methanol using Pt/α-MoC catalysts. *Nature* 2017, *544*, 80–83.

[5] Xiong, Y.; Sun, W. M.; Han, Y. H.; Xin, P. Y.; Zheng, X. S.; Yan, W. S.; Dong, J. C.; Zhang, J.; Wang, D. S.; Li, Y. D. Cobalt single atom site catalysts with ultrahigh metal loading for enhanced aerobic oxidation of ethylbenzene. *Nano Res.*, in press, DOI: 10.1007/s12274-020-3244-4.

[6] Zhang, Z. D.; Zhou, M.; Chen, Y. J.; Liu, S. J.; Wang, H. F.; Zhang, J.; Ji, S. F.; Wang, D. S.; Li, Y. D. Pd single-atom monolithic catalyst: Functional 3D structure and unique chemical selectivity in hydrogenation reaction. *Sci. China Mater.*, in press, DOI: 10.1007/s40843-020-1579-7.

[7] Li, X. Y.; Rong, H. P.; Zhang, J. T.; Wang, D. S.; Li, Y. D. Modulating the local coordination environment of single-atom catalysts for enhanced catalytic performance. *Nano Res.* 2020, *13*, 1842–1855.

[8] Zhang, N. Q.; Ye, C. L.; Yan, H.; Li, L. C.; He, H.; Wang, D. S.; Li, Y. D. Single-atom site catalysts for environmental catalysis. *Nano Res.* 2020, *13*, 3165–3182.

[9] Zhang, J.; Zheng, C. Y.; Zhang, M. L.; Qiu, Y. J.; Xu, Q.; Cheong, W. C.; Chen, W. X.; Zheng, L. R.; Gu, L.; Hu, Z. P. et al. Controlling N-doping type in carbon to boost single-atom site Cu catalyzed transfer hydrogenation of quinoline. *Nano Res.* 2020, *13*, 3082–3087.

[10] Chen, Y. J.; Gao, R.; Ji, S. F.; Li, H. J.; Tang, K.; Jiang, P.; Hu, H. B.; Zhang, Z. D.; Hao, H. G.; Qu, Q. Y. et al. Atomic-level modulation of electronic density at cobalt single-atom sites derived from metal-organic frameworks: Enhanced oxygen reduction performance. *Angew. Chem., Int. Ed.* 2021, *60*, 3212–3221.

[11] Yang, J. R.; Li, W. H.; Wang, D. S.; Li, Y. D. Single-atom materials: Small structures determine macroproperties. *Small Struct.* 2021, *2*, 2170006.

[12] Li, Z.; Chen, Y. J.; Ji, S. F.; Tang, Y.; Chen, W. X.; Li, A.; Zhao, J.; Xiong, Y.; Wu, Y. E.; Gong, Y. et al. Iridium single-atom catalyst on nitrogen-doped carbon for formic acid oxidation synthesized using a general host–guest strategy. *Nat. Chem.* 2020, *12*, 764–772.

[13] Yang, J. R.; Li, W. H.; Wang, D. S.; Li, Y. D. Electronic metal–support interaction of single-atom catalysts and applications in electrocatalysis. *Adv. Mater.* 2020, *32*, 2003300.

[14] Sykes, E. C. H.; Christopher, P. Recent advances in single-atom catalysts and single-atom alloys: Opportunities for exploring the uncharted phase space in-between. *Curr. Opin. Chem. Eng.* 2020, *29*, 67–73.

[15] Resasco, J.; DeRita, L.; Dai, S.; Chada, J. P.; Xu, M. J.; Yan, X. X.; Finzel, J.; Hanukovich, S.; Hoffman, A. S.; Graham, G. W. et al. Uniformity is key in defining structure-function relationships for atomically dispersed metal catalysts: The case of Pt/CeO_2. *J. Am. Chem. Soc.* 2020, *142*, 169–184.

[16] Lee, B. H.; Park, S.; Kim, M.; Sinha, A. K.; Lee, S. C.; Jung, E.; Chang, W. J.; Lee, K. S.; Kim, J. H.; Cho, S. P. et al. Reversible and cooperative photoactivation of single-atom Cu/TiO_2 photocatalysts. *Nat. Mater.* 2019, *18*, 620–626.

[17] Lu, Y. B.; Wang, J. M.; Yu, L.; Kovarik, L.; Zhang, X. W.; Hoffman, A. S.; Gallo, A.; Bare, S. R.; Sokaras, D.; Kroll, T. et al. Identification of the active complex for CO oxidation over single-atom Ir-on-$MgAl_2O_4$ catalysts. *Nat. Catal.* 2019, *2*, 149–156.

[18] Humphrey, N.; Bac, S.; Sharada, S. M. *Ab initio* molecular dynamics reveals new metal-binding sites in atomically dispersed Pt_1/TiO_2 catalysts. *J. Phys. Chem. C* 2020, *124*, 24187–24195.

[19] Wang, Y. G.; Mei, D. H.; Glezakou, V. A.; Li, J.; Rousseau, R. Dynamic formation of single-atom catalytic active sites on ceria-supported gold nanoparticles. *Nat. Commun.* 2015, *6*, 6511.

[20] Daelman, N.; Capdevila-Cortada, M.; López, N. Dynamic charge and oxidation state of Pt/CeO_2 single-atom catalysts. *Nat. Mater.* 2019, *18*, 1215–1221.

[21] DeRita, L.; Resasco, J.; Dai, S.; Boubnov, A.; Thang, H. V.; Hoffman, A. S.; Ro, I.; Graham, G. W.; Bare, S. R.; Pacchioni, G. et al. Structural evolution of atomically dispersed Pt catalysts dictates reactivity. *Nat. Mater.* 2019, *18*, 746–751.

[22] Tang, Y.; Asokan, C.; Xu, M. J.; Graham, G. W.; Pan, X. Q.; Christopher, P.; Li, J.; Sautet, P. Rh single atoms on TiO_2 dynamically respond to reaction conditions by adapting their site. *Nat. Commun.* 2019, *10*, 4488.

[23] Chen, Y. J.; Ji, S. F.; Sun, W. M.; Chen, W. X.; Dong, J. C.; Wen, J. F.; Zhang, J.; Li, Z.; Zheng, L. R.; Chen, C. et al. Discovering partially charged single-atom Pt for enhanced anti-markovnikov alkene hydrosilylation. *J. Am. Chem. Soc.* 2018, *140*, 7407–7410.

[24] Hoang, S.; Guo, Y. B.; Binder, A. J.; Tang, W. X.; Wang, S.; Liu, J. Y.; Tran, H.; Lu, X. X.; Wang, Y.; Ding, Y. et al. Activating low-temperature diesel oxidation by single-atom Pt on TiO_2 nanowire array. *Nat. Commun.* 2020, *11*, 1062.

[25] Macino, M.; Barnes, A. J.; Althahban, S. M.; Qu, R. Y.; Gibson, E. K.; Morgan, D. J.; Freakley, S. J.; Dimitratos, N.; Kiely, C. J.; Gao, X. et al. Tuning of catalytic sites in Pt/TiO_2 catalysts for the chemoselective hydrogenation of 3-nitrostyrene. *Nat Catal.* 2019, *2*, 873–881.

[26] Yu, F.; Wang, C. H.; Ma, H.; Song, M.; Li, D. S.; Li, Y. Y.; Li, S. M.; Zhang, X. T.; Liu, Y. C. Revisiting Pt/TiO_2 photocatalysts for thermally assisted photocatalytic reduction of CO_2. *Nanoscale* 2020, *12*, 7000–7010.

[27] Yang, M.; Liu, J. L.; Lee, S.; Zugic, B.; Huang, J.; Allard, L. F.; Flytzani-Stephanopoulos, M. A common single-site Pt(II)–$O(OH)_x$– species stabilized by sodium on "active" and "inert" supports catalyzes the water-gas shift reaction. *J. Am. Chem. Soc.* 2015, *137*, 3470–3473.

[28] Ammal, S. C.; Heyden, A. Understanding the nature and activity of supported platinum catalysts for the water–gas shift reaction: From metallic nanoclusters to alkali-stabilized single-atom cations. *ACS Catal.* 2019, *9*, 7721–7740.

[29] Chen, Y. J.; Ji, S. F.; Sun, W. M.; Lei, Y. P.; Wang, Q. C.; Li, A.; Chen, W. X.; Zhou, G.; Zhang, Z. D.; Wang, Y. et al. Engineering the atomic interface with single platinum atoms for enhanced

photocatalytic hydrogen production. *Angew. Chem., Int. Ed.* 2020, *59*, 1295–1301.

[30] Jones, J.; Xiong, H.; DeLaRiva, A. T.; Peterson, E. J.; Pham, H.; Challa, S. R.; Qi, G.; Oh, S.; Wiebenga, M. H.; Hernández, X. I. P. et al. Thermally stable single-atom platinum-on-ceria catalysts via atom trapping. *Science* 2016, *353*, 150–154.

[31] Zhang, Z. L.; Zhu, Y. H.; Asakura, H.; Zhang, B.; Zhang, J. G.; Zhou, M. X.; Han, Y.; Tanaka, T.; Wang, A. Q.; Zhang, T. et al. Thermally stable single atom Pt/m-$A_{l2}O_3$ for selective hydrogenation and CO oxidation. *Nat. Commun.* 2017, *8*, 16100.

[32] Bruix, A.; Lykhach, Y.; Matolínová, I.; Neitzel, A.; Skála, T.; Tsud, N.; Vorokhta, M.; Stetsovych, V.; Ševčíková, K.; Mysliveček, J. et al. Maximum noble-metal efficiency in catalytic materials: Atomically dispersed surface platinum. *Angew. Chem., Int. Ed.* 2014, *53*, 10525–10530.

[33] Kwak, J. H.; Hu, J.; Mei, D.; Yi, C. W.; Kim, D. H.; Peden, C. H. F.; Allard, L. F.; Szanyi, J. Coordinatively unsaturated Al^{3+} centers as binding sites for active catalyst phases of platinum on γ-Al_2O_3. *Science* 2009, *325*, 1670–1673.

[34] Diebold, U. The surface science of titanium dioxide. *Surf. Sci. Rep.* 2003, *48*, 53–229.

[35] Schaub, R.; Thostrup, P.; Lopez, N.; Lægsgaard, E.; Stensgaard, I.; Nørskov, J. K.; Besenbacher, F. Oxygen vacancies as active sites for water dissociation on rutile TiO_2(110). *Phys. Rev. Lett.* 2001, *87*, 266104.

[36] Brookes, I. M.; Muryn, C. A.; Thornton, G. Imaging water dissociation on TiO_2(110). *Phys. Rev. Lett.* 2001, *87*, 266103.

[37] He, Y. B.; Dulub, O.; Cheng, H. Z.; Selloni, A.; Diebold, U. Evidence for the predominance of subsurface defects on reduced anatase TiO_2(101). *Phys. Rev. Lett.* 2009, *102*, 106105.

[38] Cheng, H. Z.; Selloni, A. Surface and subsurface oxygen vacancies in anatase TiO_2 and differences with rutile. *Phys. Rev. B* 2009, *79*, 092101.

[39] Scheiber, P.; Fidler, M.; Dulub, O.; Schmid, M.; Diebold, U.; Hou, W. Y.; Aschauer, U.; Selloni, A. (Sub)surface mobility of oxygen vacancies at the TiO_2 anatase (101) surface. *Phys. Rev. Lett.* 2012, *109*, 136103.

[40] Jin, C.; Dai, Y.; Wei, W.; Ma, X. C.; Li, M. M.; Huang, B. B. Effects of single metal atom (Pt, Pd, Rh, and Ru) adsorption on the photocatalytic properties of anatase TiO_2. *Appl. Surf. Sci.* 2017, *426*, 639–646.

[41] Delley, B. An all-electron numerical method for solving the local density functional for polyatomic molecules. *J. Chem. Phys.* 1990, *92*, 508–517.

[42] Delley, B. From molecules to solids with the $DMol^3$ approach. *J. Chem. Phys.* 2000, *113*, 7756–7764.

[43] Wang, X. Y.; Zhang, L.; Bu, Y. X.; Sun, W. M. Interplay between invasive single atom Pt and native oxygen vacancy in anatase TiO_2(101) surface: A theoretical study. *Appl. Surf. Sci.* 2021, *540*, 148357.

[44] Hammer, B.; Hansen, L. B.; Nørskov, J. K. Improved adsorption energetics within density-functional theory using revised Perdew–Burke–Ernzerhof functionals. *Phys. Rev. B* 1999, *59*, 7413–7421.

[45] Delley, B. Hardness conserving semilocal pseudopotentials. *Phys. Rev. B* 2002, *66*, 155125.

[46] Li, Y. D.; Gao, Y. Interplay between water and TiO_2 anatase (101) surface with subsurface oxygen vacancy. *Phys. Rev. Lett.* 2014, *112*, 206101.

[47] Cromer, D. T.; Herrington, K. The structures of anatase and rutile. *J. Am. Chem. Soc.* 1955, *77*, 4708–4709.

[48] Govind, N.; Petersen, M.; Fitzgerald, G.; King-Smith, D.; Andzelm, J. A generalized synchronous transit method for transition state location. *Comput. Mater. Sci.* 2003, *28*, 250–258.

[49] Luo, Z. B.; Wang, Z. J.; Li, J.; Yang, K.; Zhou, G. N-promoted Ru1/TiO_2 single-atom catalysts for photocatalytic water splitting for hydrogen production: A density functional theory study. *Phys. Chem. Chem. Phys.* 2020, *22*, 11392–11399.

[50] Prandini, G.; Marrazzo, A.; Castelli, I. E.; Mounet, N.; Marzari, N. Precision and efficiency in solid-state pseudopotential calculations. *npj Comput. Mater.* 2018, *4*, 72.

[51] Lejaeghere, K.; Bihlmayer, G.; Björkman, T.; Blaha, P.; Blügel, S.; Blum, V.; Caliste, D.; Castelli, I. E.; Clark, S. J.; Dal Corso, A. et al. Reproducibility in density functional theory calculations of solids. *Science* 2016, *351*, aad3000.

[52] Giannozzi, P.; Baroni, S.; Bonini, N.; Calandra, M.; Car, R.; Cavazzoni, C.; Ceresoli, D.; Chiarotti, G. L.; Cococcioni, M.; Dabo, I. et al. Quantum Espresso: A modular and open-source software project for quantum simulations of materials. *J. Phys.: Condens. Matter* 2009, *21*, 395502.

[53] Giannozzi, P.; Andreussi, O.; Brumme, T.; Bunau, O.; Nardelli, M. B.; Calandra, M.; Car, R.; Cavazzoni, C.; Ceresoli, D.; Cococcioni, M. et al. Advanced capabilities for materials modelling with Quantum Espresso. *J. Phys.: Condens. Matter* 2017, *29*, 465901.

[54] Cococcioni, M.; de Gironcoli, S. Linear response approach to the calculation of the effective interaction parameters in the LDA + U method. *Phys. Rev. B* 2005, *71*, 035105.

[55] Deskins, N. A.; Rousseau, R.; Dupuis, M. Distribution of Ti^{3+} surface sites in reduced TiO_2. *J. Phys. Chem. C* 2011, *115*, 7562–7572.

[56] Johnson, E. R.; Keinan, S.; Mori-Sánchez, P.; Contreras-García, J.; Cohen, A. J.; Yang, W. T. Revealing noncovalent interactions. *J. Am. Chem. Soc.* 2010, *132*, 6498–6506.

[57] Lu, T.; Chen, F. W. Multiwfn: A multifunctional wavefunction analyzer. *J. Comput. Chem.* 2012, *33*, 580–592.

[58] Sun, W. M.; Di Felice, R. Nature of the interaction between natural and size-expanded guanine with gold clusters: A density functional theory study. *J. Phys. Chem. C* 2012, *116*, 24954–24961.

[59] Matsunaga, K.; Chang, T. Y.; Ishikawa, R.; Dong, Q.; Toyoura, K.; Nakamura, A.; Ikuhara, Y.; Shibata, N. Adsorption sites of single noble metal atoms on the rutile TiO_2(110) surface influenced by different surface oxygen vacancies. *J. Phys.: Condens. Matter* 2016, *28*, 175002.

[60] Zhang, Z. R.; Ge, Q. F.; Li, S. C.; Kay, B. D.; White, J. M.; Dohnálek, Z. Imaging intrinsic diffusion of bridge-bonded oxygen vacancies on TiO_2(110). *Phys. Rev. Lett.* 2007, *99*, 126105.

[61] Helali, Z.; Markovits, A.; Minot, C.; Abderrabba, M. Metal atom adsorption on a defective TiO_{2-x} support. *Chem. Phys. Lett.* 2014, *594*, 23–29.

[62] Tauster, S. J. Strong metal-support interactions. *Acc. Chem. Res.* 1987, *20*, 389–394.

[63] Hwang, J.; Noh, S. H.; Han, B. Design of active bifunctional electrocatalysts using single atom doped transition metal dichalcogenides. *Appl. Surf. Sci.* 2019, *471*, 545–552.

[64] Han, B. C.; Van der Ven, A.; Ceder, G.; Hwang, B. J. Surface segregation and ordering of alloy surfaces in the presence of adsorbates. *Phys. Rev. B* 2005, *72*, 205409.

[65] Noh, S. H.; Kwon, C.; Hwang, J.; Ohsaka, T.; Kim, B. J.; Kim, T. Y.; Yoon, Y. G.; Chen, Z. W.; Seo, M. H.; Han, B. Self-assembled nitrogen-doped fullerenes and their catalysis for fuel cell and rechargeable metal–air battery applications. *Nanoscale* 2017, *9*, 7373–7379.

[66] Chen, X.; McDonald, A. R. Functionalization of two-dimensional transition-metal dichalcogenides. *Adv. Mater.* 2016, *28*, 5738–5746.